APL Materials

Strain-tunable III-nitride/ZnO heterostructures for photocatalytic water-splitting: A hybrid functional calculation

Cite as: APL Mater. **8**, 041114 (2020); https://doi.org/10.1063/5.0005648
Submitted: 23 February 2020 . Accepted: 03 April 2020 . Published Online: 20 April 2020

Zhaofu Zhang, Bingquan Huang, Qingkai Qian, Zhibin Gao, Xi Tang, and Baikui Li

AIP Publishing

Strain-tunable III-nitride/ZnO heterostructures for photocatalytic water-splitting: A hybrid functional calculation

Cite as: APL Mater. 8, 041114 (2020); doi: 10.1063/5.0005648
Submitted: 23 February 2020 • Accepted: 3 April 2020 •
Published Online: 20 April 2020

Zhaofu Zhang,[1,a)] Bingquan Huang,[2] Qingkai Qian,[3] Zhibin Gao,[4] Xi Tang,[2] and Baikui Li[2,a)]

AFFILIATIONS

[1]Department of Engineering, University of Cambridge, Cambridge CB2 1PZ, United Kingdom
[2]College of Physics and Optoelectronic Engineering, Shenzhen University, Shenzhen 518060, China
[3]Department of Electrical Engineering, The Pennsylvania State University, University Park, Pennsylvania 16802, USA
[4]Department of Physics, National University of Singapore, Singapore 117551, Republic of Singapore

Note: This paper is part of the Special Issue on Solar to Fuel.
[a)]**Authors to whom correspondence should be addressed:** zz389@cam.ac.uk and libk@szu.edu.cn

ABSTRACT

Solar to fuel energy conversion is one of the momentous topics nowadays considering the urgent demand for clean energy supplies. In this work, the tunable electronic and optical properties of III-nitride/ZnO 2D/2D heterostructures (including GaN/ZnO, AlN/ZnO, and GaN/AlN) by strain engineering were investigated by first-principles calculations. The studied heterostructures feature a small interlayer distance, with the cation of one layer directly above the anion of the other layer, and vice versa. This leads to a strong binding energy and interlayer coupling across the heterostructure. The built-in field induced by the charge redistribution facilitates the photoexcited carrier migration, which is beneficial to the photocatalytic water splitting application. The stable III-nitride/ZnO heterostructures exhibit decent band edge positions with biaxial strain engineering and feature an enhancement of optical absorption under tensile strain. Our results indicate that the III-nitride/ZnO 2D/2D heterostructures are promising photocatalysts for solar to hydrogen generation by water splitting.

I. INTRODUCTION

With the rapid development of the contemporary industry, fossil fuel is being extensively consumed, which can lead to serious environmental issues. It is now a mainstream issue to find sufficient renewable and clean energy supplies. Solar to fuel is a technologically feasible approach to effectively tackle the energy crisis.[1,2] Photocatalytic water splitting using semiconductors as catalysts to generate hydrogen stands out as a sustainable strategy for the generation of solar energy.[3,4] For high-efficiency photocatalyst in solar energy conversion applications, reasonable band edge positions with the respect to water redox potentials and suitable bandgap values are required.[5] In addition, the photo-excited electrons and holes should possess a long lifetime for effective separation to improve the water splitting efficiency.[6–8] Two-dimensional (2D) semiconductor materials with the high surface area–volume ratio, low defect concentration, and tunable bandgap value are promising candidates for high-efficiency photocatalytic water-splitting.

Wide bandgap semiconductors of ZnO, GaN, and AlN have attracted increasing attention for optoelectronic and power electronic applications.[9–12] Meanwhile, research studies on their 2D structures are also proceeding rapidly and productively,[13–16] ever since the successful experimental synthesis of their graphene-like 2D counterparts.[17–19] For example, Tusche *et al.*[17] successfully observed the unreconstructed planar sheet of g-ZnO monolayers grown on metal substrates. The energetic and dynamic stability of 2D Group-III nitride (III-nitride) was first investigated by first-principle calculations,[20] which was later experimentally synthesized.[18,19] Numerous

investigations have been conducted on the photocatalytic water-splitting application of 2D GaN, AlN, and ZnO, as well as their heterostructures with other 2D materials by either theoretical[21–31] or experimental[32,33] approaches. Considering that 2D GaN, AlN, and ZnO share the same graphene-like honeycomb configuration and a negligible difference of the lattice constant (3.1–3.2 Å), it is straightforward to come up with the idea of combining their mutual heterostructures and exploring the potential photocatalytic applications. Despite some reports on their heterostructures, i.e., GaN/ZnO[34–36] and AlN/ZnO,[35,37] the reported details remain controversial and a thorough understanding is still lacking. Besides, there has been no report on the properties of the 2D GaN/AlN heterostructure, which could also be adopted for solar-to-fuel energy conversion photocatalysts.

In this work, we investigated the electronic and optical properties of the 2D/2D heterostructures of GaN/ZnO, AlN/ZnO, and GaN/AlN by first-principles calculations. To guarantee the accuracy of our results, the hybrid functional was adopted. With biaxial strain engineering, the tunable band structures and optical absorption were studied. In contrast to a typical van der Waals (vdW) heterostructure with an interlayer distance of ~3 Å or larger, the studied III-nitride/ZnO heterostructures feature a smaller interlayer distance of 2.1–2.3 Å and, consequently, a much larger binding energy. The cation at one side is directly on top of the anion at the other side and vice versa. This leads to the electron overlapping within the heterostructure, verified by the charge density difference and electrostatic potential across the heterostructure. The studied heterostructures show indirect bandgap characteristics, with the conduction band minimum (CBM) at the Γ point and valence band maximum (VBM) at the K point, and the band edges are contributed by both materials. The band edge positions in a wide strain range always span the water redox potentials, and the optical absorption ability could be greatly enhanced by strain engineering. These tunable properties suggest that the heterostructures among GaN, AlN, and ZnO monolayers have attractive application potentials for photocatalytic applications for hydrogen production.

II. CALCULATION METHODS

All the calculations in this work were conducted based on density functional theory (DFT) implemented in the VASP code.[38] The projected augmented wave potential (PWA)[39] was adopted with a plane-wave cut-off energy of 520 eV. The convergence criteria were set to be of 1×10^{-5} eV/atom for energy and 0.01 eV/Å for the residual forces on each atom. An $11 \times 11 \times 1$ k-mesh grid was used for the Brillouin zone integration. The vdW correction with Grimme's scheme (DFT-D3) was considered.[40] A 20 Å thickness vacuum layer was adopted to avoid interaction between imaged layers along the z-direction.[41] VASPKIT, a pre- and post-processing program for the VASP code,[42] was used for the analysis of band structures.

It should be noted that despite the wide use of the Perdew-Burke-Ernzerhof version of generalized gradient approximation (GGA-PBE) exchange-correlation functional[43] for calculations, it suffers from the slightly overestimated lattice constant and unavoidable bandgap narrowing problems,[44] which significantly impact the properties of 2D materials. Here, we employed the Heyd-Scuseria-Ernzerhof (HSE) hybrid functional[45] throughout the work, including the lattice structure optimization and electronic and optical property calculations, to guarantee the precise property acquisitions.[46] Previous work by Wang *et al.* adopted the 10% HF mixing fraction for III-nitride and 17.5% for the heterostructures,[36,37] which, however, underestimated the bandgaps of GaN and AlN (2.70 eV[36] and 3.36 eV[37] in their reports) monolayers or their heterostructures, inconsistent with previous reports.[21] The experimental bandgaps for 2D GaN and AlN are 5.0 eV[18] and 9.2 eV,[19] respectively, larger than their 3D counterparts. However, it is noted that experimental 2D III-nitride was sandwiched between graphene and the silicon substrate, rather than the freestanding case, and they are not exactly the graphene-like honeycomb phase, so it is not necessary to use a significantly higher HF fraction to perfectly reproduce the reported gap values. With the overall consideration, we insist to use the default HF fraction (25%) in the HSE functional to obtain the reasonable electronic structures.

III. RESULTS AND DISCUSSIONS

The monolayer material properties, calculated by PBE and HSE functionals, are summarized in Table I for comparison. Obviously, the PBE derived lattice constant is slightly larger than that derived by the HSE functional, consistent with the previous reports.[44,46] The calculated monolayer material bandgap by the PBE functional is obviously smaller than the HSE one, suffering from the well-known bandgap narrowing problem by the semi-local exchange-correlation functional. Both functionals give close gap values to previous reports. To guarantee more accuracy, the HSE functional is adopted in all the later heterostructure calculations, including the heterostructure relaxation, and electronic and optical property characterizations. The 2D materials studied here are a graphene-like honeycomb structure with sp^2 hybridization, different from their 3D counterparts that feature a wurtzite or zinc blende structure with sp^3 hybridization. This explains that the calculated bandgap energies of these 2D materials are not necessarily larger than those of the bulk ones.

The calculated bandgap of the GaN, AlN, and ZnO monolayer is 3.48 eV, 4.11 eV, and 3.30 eV, respectively, as shown in Fig. 1. The GaN and AlN monolayers are indirect-bandgap semiconductors, with the conduction band minimum (CBM) at the Γ point and valence band maximum (VBM) at the K point. The nitrogen atom, especially the N–p orbital, contributes the most to the valence band regions near VBM, while Ga (Al) contributes more to the conduction band. 2D ZnO is a direct-bandgap material with band edges at the Γ point.

The lattice constants of the three materials are very similar, ranging from 3.10 Å to 3.25 Å shown in Table I. Lattice mismatches of GaN/ZnO, AlN/ZnO, and GaN/AlN heterostructures are 0.62%,

TABLE I. Lattice constant and bandgap (Eg) comparison between PBE functional and HSE functional on GaN, AlN, and ZnO monolayer.

	Lattice constant (Å)		E_g (eV)		E_g in References (eV)	
Monolayer	PBE	HSE	PBE	HSE	PBE	HSE
GaN	3.24	3.21	1.98	3.48	~2.00[22]	~3.20[31]
AlN	3.12	3.10	2.92	4.11	~2.90[22,23]	~4.05[22,23]
ZnO	3.29	3.25	1.65	3.30	~1.69[30]	~3.29[28]

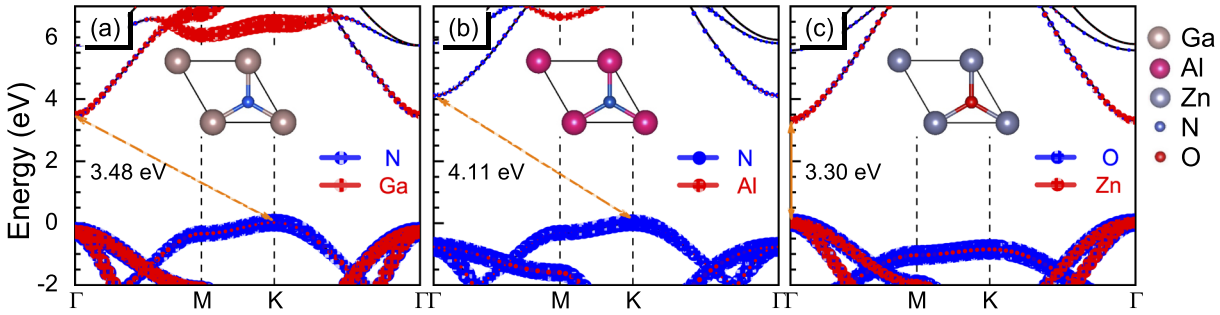

FIG. 1. Projected band structures for (a) GaN, (b) AlN, and (c) ZnO monolayers by the HSE functional, respectively. The VBM in the band structure is set to be 0 eV. Insets: the corresponding atomic unit cells.

2.36%, and 1.74%, respectively, according to the HSE derived lattice constants. The proposed interface configurations of III-N/ZnO heterostructures are formed within a 3% lattice mismatch. Considering that DFT cannot guarantee the global minimum, the six most possible 2D/2D configurations for III-nitride/ZnO heterostructures with different high-symmetry atomic arrangements are modeled, as we have done in the previous report.[7] The six configurations for GaN/ZnO are shown in Fig. 2, where the special rotation angle has been considered. We used the averaged lattice constant of the two components for initial interface modeling. Different initial layer distance is tested, with the relative energy mapping diagram shown in Fig. 3.

Clearly, the six different models have similar energy distribution trends in three kinds of III-nitride/ZnO heterostructures, while the Type-III alignment has been the most energy-stable configuration, indicating most likely that the experimentally synthesized structure shows such an atomic arrangement. As a result, we only focus on the Type-III case in further discussions, since it is less meaningful to dive into other configurations with a low possibility.

The cell vectors during relaxation calculations are optimized to ensure that all the atomic configurations are fully relaxed. The lattice information of relaxed GaN/ZnO, AlN/ZnO, and GaN/AlN heterostructures is summarized in Table II. The interlayer distance is 2.1–2.3 Å, much smaller than that of the typical vdW heterostructure. This is because the studied Type-III structure is constructed in the 1 × 1 cell, with the cation at one side directly on top of the anion at the other side, leading to a strong interlayer coupling, thus reducing the distance. Small distance is also reported in previous work,[34,35] despite their relaxation is conducted by the PBE functional. The binding energy values (see Table II) are negative, indicating the exothermic process during the heterostructure formation. It is noted that the strong interlayer interaction releases more energy, leading to much larger binding energy than the typical vdW binding energy of ~20 meV/Å^2,[47] further confirming that these are non-typical heterostructures rather than the vdW heterostructure, as described in Ref. 35. Taking GaN/ZnO, for example, the binding energy (−70.45 meV/Å^2) in our work is more negative than the reports (−50 meV/Å^2 to −60 meV/Å^2),[34–36] induced by

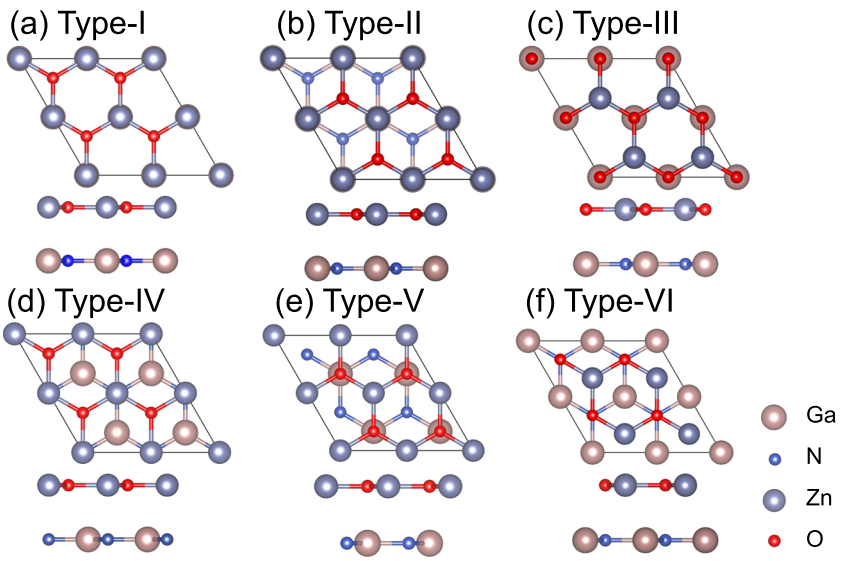

FIG. 2. Schematic views of GaN/ZnO heterostructures with various high-symmetry atomic arrangements, shown in a (2 × 2) supercell. Both the top view and side view are given. (a)–(f) are labeled Type-I to Type-VI, respectively. The same modeling strategies also suit AlN/ZnO and GaN/AlN cases.

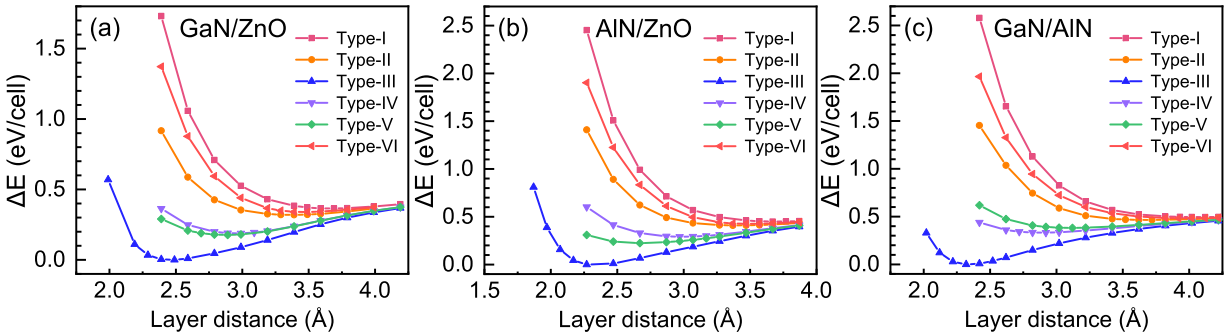

FIG. 3. Layer distance mapping [(a)–(c)] for the six type heterostructures to identify the most energy-stable configurations. Obviously, type-III shows the most energy-stable feature for all heterostructures.

the different functional adopted. An even stronger binding phenomenon can be observed in AlN/ZnO and GaN/AlN heterostructures, owing to the relatively smaller interlayer distance. As a result, the studied heterostructures can all be stably synthesized when the experiment condition becomes mature in the future.

Figure 4 shows the projected band structures of the studied 2D/2D heterostructures, where the indirect-bandgap structures are shown, with CBM at the Γ point and VBM at the K point. Such indirect bandgap characteristics prevent the recombination of photoexcited holes and electrons, leading to a long carrier lifetime, which is beneficial to solar energy conversion applications.[7,48] The contributions from both materials can be observed at CBM and VBM, as verified by the projected band structures in Fig. 4. This indicates that the interlayer wavefunction overlaps exist in both VB and CB, owing to the small interlayer distance, thus the strong interlayer coupling and orbital hybridization. Meanwhile, the bandgap of AlN/ZnO (and GaN/AlN) is 3.40 eV (3.61 eV), which is 0.1 eV larger than that of the isolated ZnO (GaN), resulting from the strong interlayer orbital hybridization. Considering this, it is less meaningful to claim this heterostructure as the "type-II" band alignment, as in Ref. 35. Especially, the band offset in Ref. 35 is only 6 meV and 88 meV. With such a small band offset, the band edges from both materials actually hybridize with each other.

The charge density difference diagram[49] in Fig. 5 also validates the interlayer charge redistribution and orbital hybridization. It is obvious that the electrons from the cation (cyan isosurface, depleted charge) of one side transfer to the anion (yellow isosurface, accumulated charge) of the other side, leading to the charge transfer across the interface. Bader charge analysis[41,50] proves a 0.04 |e|/unitcell interface charge transfer from ZnO to GaN, leading to the potential drop (ΔV) across the interface, as shown in the averaged-potential curve in Fig. 5(d). The Bader charge transfer for AlN/ZnO and GaN/AlN is larger (0.23 and 0.24 |e|/unitcell, respectively), owing to the relatively smaller interlayer distance and stronger orbital hybridization. The potential drop leads to the intrinsic built-in potential, which will contribute to the carrier migration across the heterostructure. The photogenerated carriers can be separated by the built-in potential, which is beneficial for the enhanced photocatalytic water splitting capability.

TABLE II. The lattice constant, interlayer distance, binding energy (E_b), and bandgap of the final relaxed Type-III heterostructure. The binding energy is calculated by equations adopted in Refs. 21 and 35.

Heterostructure	Lattice constant (Å)	Distance (Å)	E_b (meV/Å^2)	E_g (eV)
GaN/ZnO	3.29	2.29–2.32	−70.45	3.28
AlN/ZnO	3.25	2.15–2.22	−91.98	3.40
GaN/AlN	3.23	2.15–2.21	−102.23	3.61

Strain engineering is an effective method to tune the electronic structures and bandgaps of 2D materials. In calculation, the strain is introduced by adjusting the cell lattice constants, relaxing the atom coordinates, and analyzing the corresponding electronic structures.[14,51] Practically, strain engineering can be realized by growing or transferring the 2D heterostructures on a flexible substrate that can be starched or compressed. Biaxial strain engineering is applied to systematically study the electronic properties, which is tuned from the smallest compressive strain of −6% to the largest tensile strain of 6%. Here, the strain-dependent band structures of the GaN/ZnO heterostructure are shown in Fig. 6, while those of AlN/ZnO and GaN/AlN are only summarized in Fig. 7 below. The relaxed (no strain case) GaN/ZnO is an indirect bandgap semiconductor [Fig. 4(a)]. The direct–indirect transition of the bandgap can be observed from a compressive strain to a tensile strain. Besides, bandgap values change simultaneously. The CBM always lies in the Γ point, while VBM changes from Γ (with compressive strain) to K (with tensile strain). With a decrease in compressive strain (from −6% to zero strain) and an increase in tensile strain (from zero strain to +6%), the bandgap value increases first and then becomes smaller, resulting from the varied band edge positions under different strain. The GaN/ZnO bandgap value reaches a maximum of 3.55 eV with a −4% compressive strain.

By the deployment of strain engineering, the tunable band edge positions for the three heterostructures are summarized in Fig. 7. The accurate band edge positions here are obtained using the core level alignment scheme[7,52,53] and referred to the vacuum level. The reduction potential of H^+/H_2 (−4.44 eV, with respect to the vacuum level) and the oxidation potential of H_2O/O_2 (−5.67 eV) are labeled. It is clear that even with the tensile or compressive strain (except

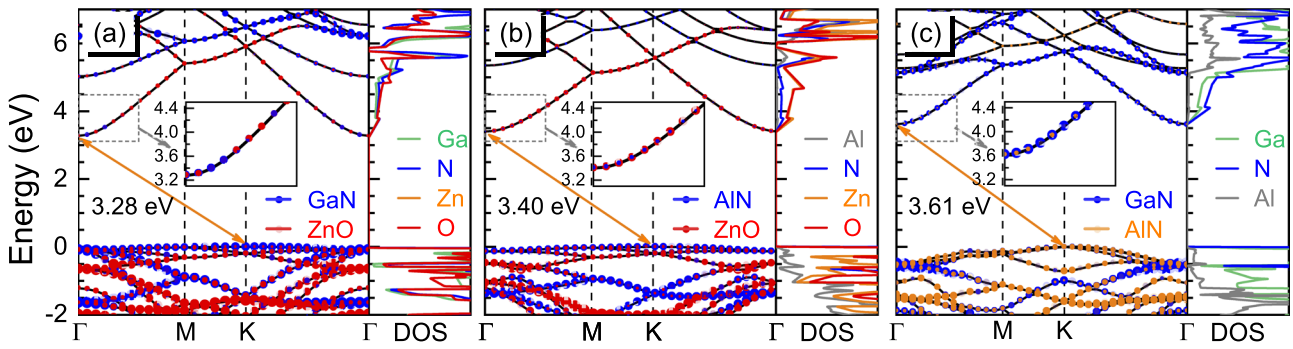

FIG. 4. Projected band structures and density of states (DOS) for (a) GaN/ZnO, (b) AlN/ZnO, and (c) GaN/AlN heterostructures, respectively. The VBM is set to be 0 eV. The zoomed-in view of CBM is shown in the inset of each figure.

for −6% for GaN/ZnO), the studied heterostructures all show decent band edge positions that straddle the redox potentials of H^+/H_2 and O_2/H_2O, showing the excellent strain-tolerance for splitting water to generate O_2 and H_2.

The optical properties of semiconductors are related to their electronic structures. Here, the strain-dependent optical absorption spectra are shown in Fig. 8 using the absorption coefficient formula[7] $\alpha(E) = (\sqrt{2}\omega/c)\{[(\varepsilon_1^2+\varepsilon_2^2)^{1/2}-\varepsilon_1]\}^{1/2}$, where ε_1 and ε_2 are the real and imaginary parts of the complex dielectric function. Clearly, with the increase in tensile strain, the heterostructures show an enhanced optical absorption ability, especially in the solar region and solar-blind region, owing to the reduced bandgap value. Combining with the band edge line-up in Fig. 7, even under tensile strain (reduced gap), the band edges in the studied heterostructures still span the redox potentials. For example, if 6% lattice distortion is applied, the absorption capacity is increased by several times and

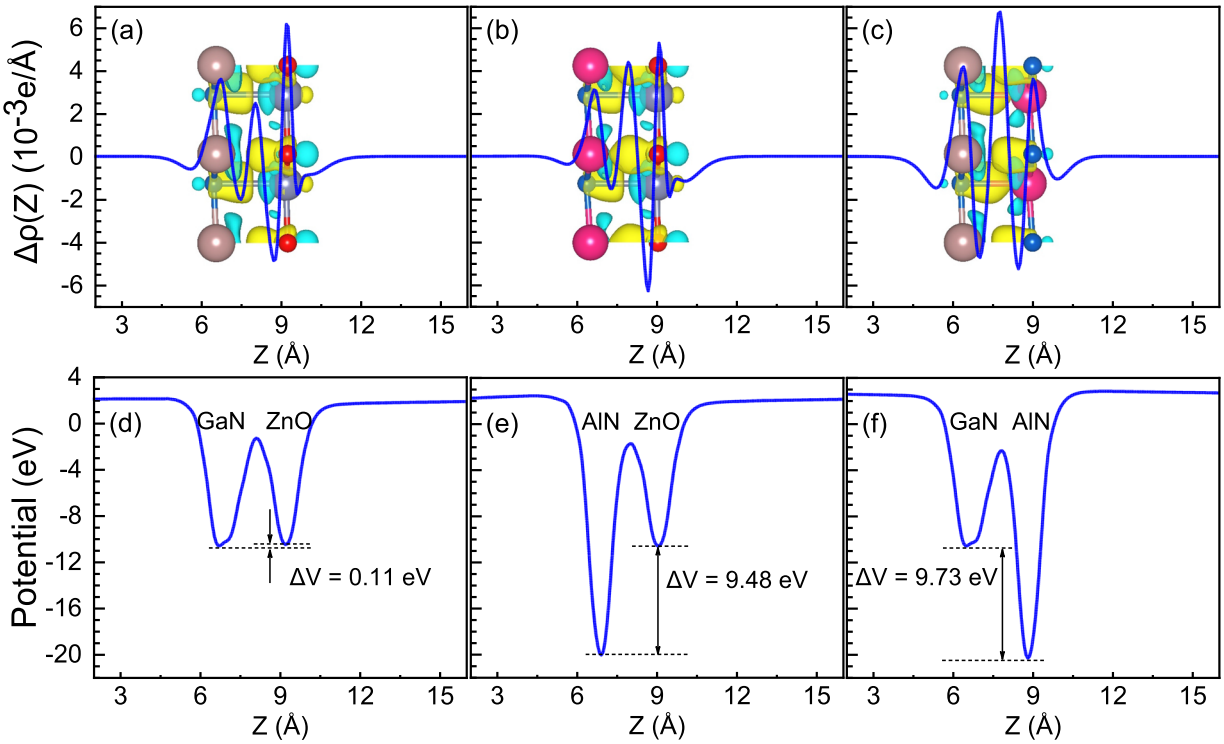

FIG. 5. [(a)–(c)] Charge density difference and [(d)–(f)] planer averaged potential curves for GaN/ZnO, AlN/ZnO, and GaN/AlN heterostructures, respectively. The cyan and yellow charge densities indicate charge depletion and accumulation, respectively.

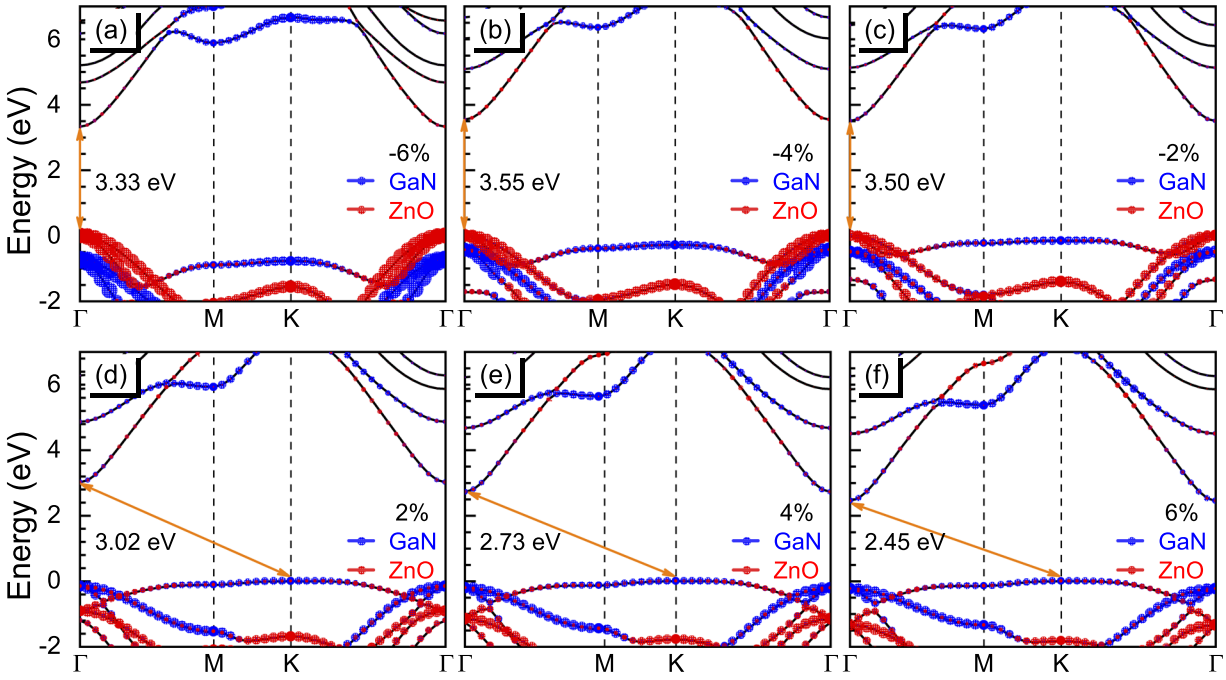

FIG. 6. Strain dependent band structures [(a)–(f)] of the GaN/ZnO heterostructure. The band structure for no strain case is already shown in Fig. 4(a).

the band edge positions are still ideal for water dissociation, which proves that the studied heterostructures can be used as an excellent photo-absorber in tandem with other narrow bandgap semiconductors for high-efficiency photocatalytic water splitting.[7] In a 2D/2D heterostructure, there are two kinds of absorption processes: (i) intralayer absorption and (ii) interlayer absorption. The intralayer VB-to-CB absorption or the below-bandgap excitonic absorption[54] generates intralayer excitons. The intralayer excitons, although with

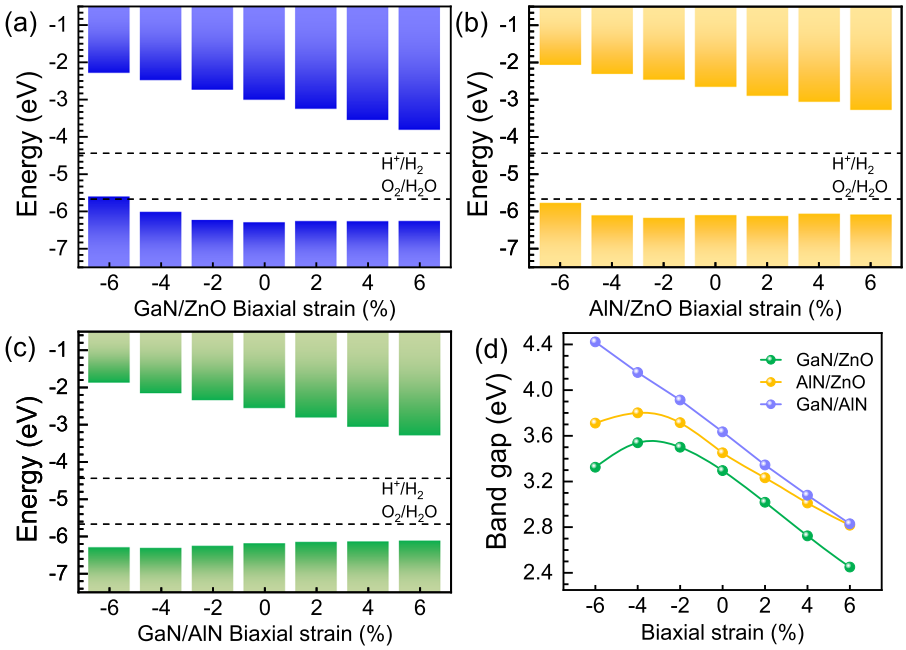

FIG. 7. Strain-dependent band edge positions. (a) GaN/ZnO, (b) AlN/ZnO, and (c) GaN/AlN heterostructures with reference to the vacuum level. (d) Bandgap values vs applied biaxial strain for the corresponding heterostructures.

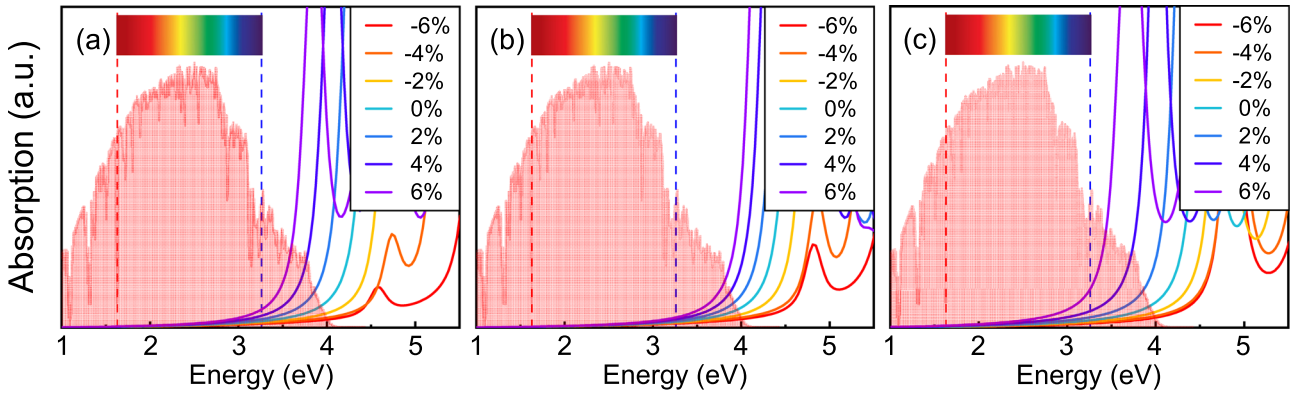

FIG. 8. Strain-dependent optical absorption spectra of (a) GaN/ZnO, (b) AlN/ZnO, and (c) GaN/AlN heterostructures, respectively. The solar radiation spectrum, downloaded from the NERL website (http://www.nrel.gov/solar_radiation/), is shown for reference.

a binding energy up to hundreds of meV, may dissociate at the heterointerface, taking the band offset as an energy compensation.[55] The interlayer absorption, with electrons excited from the VB of one layer to the CB of the other layer, generates interlayer excitons. The interlayer exciton, which has a much smaller binding energy than that of the interlayer exciton,[56] is easy to dissociate and contributes to water splitting.

IV. CONCLUSION

In summary, we systemically studied the 2D/2D heterostructures of GaN/ZnO, AlN/ZnO, and GaN/AlN to evaluate their photocatalytic capability by first-principles calculation. We find that, in contrast to the widely reported van der Waals heterostructures, these wide bandgap semiconductor 2D heterostructures show a much smaller layer distance as well as a stronger interlayer interaction and charge transfer. The charge density redistribution results in the built-in field, which boosts the photoexcited carrier transfer. These heterostructures show excellent strain-tolerance with suitable band edge positions and enhanced optical absorption ability with a tensile strain. The calculated results indicate that the III-nitride/ZnO heterostructures are promising for solar to fuel energy conversion applications as an excellent photocatalyst and could also have potential applications in flexible strain sensing and photodetectors.

AUTHOR'S CONTRIBUTIONS

Z.Z. and B.H. contributed equally to this work.

ACKNOWLEDGMENTS

This work was supported by the National Natural Science Foundation of China (Grant No. 61604098), the Shenzhen Science and Technology Innovation Commission (Grant Nos. JCYJ20170412110137562 and JCYJ20170302143001451), Key Project of Science and Technology of Guangdong Province (Grant No. 2020B010169003), and the Shenzhen University Scientific Research Start-up Foundation (Grant No. 860-000002110207). Z. Gao acknowledges financial support from MOE tier 1 funding of NUS Faculty of Science, Singapore (Grant No. R-144-000-402-114).

The data that support the findings of this study are available from the corresponding author upon reasonable request.

REFERENCES

[1] M. G. Walter, E. L. Warren, J. R. McKone, S. W. Boettcher, Q. Mi, E. A. Santori, and N. S. Lewis, Chem. Rev. **110**, 6446 (2010).
[2] C. Jiang, S. J. A. Moniz, A. Wang, T. Zhang, and J. Tang, Chem. Soc. Rev. **46**, 4645 (2017).
[3] X. Chen, S. Shen, L. Guo, and S. S. Mao, Chem. Rev. **110**, 6503 (2010).
[4] T. Hisatomi, J. Kubota, and K. Domen, Chem. Soc. Rev. **43**, 7520 (2014).
[5] A. Kudo and Y. Miseki, Chem. Soc. Rev. **38**, 253 (2009).
[6] J. S. Jang, H. G. Kim, and J. S. Lee, Catal. Today **185**, 270 (2012).
[7] Z. Zhang, Q. Qian, B. Li, and K. J. Chen, ACS Appl. Mater. Interfaces **10**, 017419 (2018).
[8] R. Meng, X. Sun, D. Yang, J. Bao, and X. Chen, Appl. Mater. Today **13**, 276 (2018); H. Cui, K. Zheng, Y. Zhang, H. Ye, and X. Chen, IEEE Electron Device Lett. **39**, 284 (2018); K. Zheng, X. Yang, H. Cui, Q. Yang, H. Ye, D. Xiong, S. Ingebrandt, and X. Chen, J. Mater. Chem. C **6**, 4943 (2018).
[9] Ü. Özgür, Y. I. Alivov, C. Liu, A. Teke, M. A. Reshchikov, S. Doğan, V. Avrutin, S.-J. Cho, and H. Morkoç, J. Appl. Phys. **98**, 041301 (2005).
[10] K. J. Chen, O. Haberlen, A. Lidow, C. L. Tsai, T. Ueda, Y. Uemoto, and Y. Wu, IEEE Trans. Electron Devices **64**, 779 (2017).
[11] J. Y. Tsao, S. Chowdhury, M. A. Hollis, D. Jena, N. M. Johnson, K. A. Jones, R. J. Kaplar, S. Rajan, C. G. Van de Walle, E. Bellotti, C. L. Chua, R. Collazo, M. E. Coltrin, J. A. Cooper, K. R. Evans, S. Graham, T. A. Grotjohn, E. R. Heller, M. Higashiwaki, M. S. Islam, P. W. Juodawlkis, M. A. Khan, A. D. Koehler, J. H. Leach, U. K. Mishra, R. J. Nemanich, R. C. N. Pilawa-Podgurski, J. B. Shealy, Z. Sitar, M. J. Tadjer, A. F. Witulski, M. Wraback, and J. A. Simmons, Adv. Electron. Mater **4**, 1600501 (2018).
[12] X. Tang, B. Li, H. A. Moghadam, P. Tanner, J. Han, and S. Dimitrijev, IEEE Electron Device Lett. **39**, 1145 (2018).
[13] Z.-F. Zhang, T.-G. Zhou, H.-Y. Zhao, and X.-L. Wei, Chin. Phys. B **23**, 016801 (2014).
[14] X. Liu, Z. Zhang, Z. Luo, B. Lv, and Z. Ding, Nanomaterials **9**, 1674 (2019).
[15] D. Kecik, A. Onen, M. Konuk, E. Gürbüz, F. Ersan, S. Cahangirov, E. Aktürk, E. Durgun, and S. Ciraci, Appl. Phys. Rev. **5**, 011105 (2018).
[16] B. Huang, T. Zhou, D. Wu, Z. Zhang, and B. Li, Acta Phys. Sin. **68**, 246301 (2019).
[17] C. Tusche, H. L. Meyerheim, and J. Kirschner, Phys. Rev. Lett. **99**, 026102 (2007).

[18]Z. Y. Al Balushi, K. Wang, R. K. Ghosh, R. A. Vilá, S. M. Eichfeld, J. D. Caldwell, X. Qin, Y.-C. Lin, P. A. DeSario, G. Stone, S. Subramanian, D. F. Paul, R. M. Wallace, S. Datta, J. M. Redwing, and J. A. Robinson, Nat. Mater. **15**, 1166 (2016).
[19]W. Wang, Y. Zheng, X. Li, Y. Li, H. Zhao, L. Huang, Z. Yang, X. Zhang, and G. Li, Adv. Mater. **31**, 1803448 (2019).
[20]H. L. Zhuang, A. K. Singh, and R. G. Hennig, Phys. Rev. B **87**, 165415 (2013).
[21]J. Liao, B. Sa, J. Zhou, R. Ahuja, and Z. Sun, J. Phys. Chem. C **118**, 017594 (2014).
[22]H. Zhang, Y.-N. Zhang, H. Liu, and L.-M. Liu, J. Mater. Chem. A **2**, 015389 (2014).
[23]Q. Yang, S. Zhang, C. Tan, H. Ye, X. Ming, S. Ingebrandt, and X. Chen, J. Mater. Chem. C **5**, 9412 (2017).
[24]M. Sun, J.-P. Chou, J. Yu, and W. Tang, Phys. Chem. Chem. Phys. **19**, 017324 (2017).
[25]Q. Yang, C.-J. Tan, R.-S. Meng, J.-K. Jiang, Q.-H. Liang, X. Sun, D.-G. Yang, and X. Chen, IEEE Electron Device Lett. **38**, 145 (2017).
[26]X. Niu, Y. Li, H. Shu, X. Yao, and J. Wang, J. Phys. Chem. C **121**, 3648 (2017).
[27]Q. Fang, Y. Huang, Y. Miao, K. Xu, Y. Li, and F. Ma, J. Phys. Chem. C **121**, 6605 (2017).
[28]S. Wang, H. Tian, C. Ren, J. Yu, and M. Sun, Sci. Rep. **8**, 012009 (2018).
[29]X. Gao, Y. Shen, Y. Ma, S. Wu, and Z. Zhou, J. Mater. Chem. C **7**, 4791 (2019).
[30]K. Ren, J. Yu, and W. Tang, J. Appl. Phys. **126**, 065701 (2019).
[31]K. Ren, Y. Luo, S. Wang, J.-P. Chou, J. Yu, W. Tang, and M. Sun, ACS Omega **4**, 021689 (2019).
[32]Y. Liu, H. Liu, H. Zhou, T. Li, and L. Zhang, Appl. Surf. Sci. **466**, 133 (2019).
[33]J. Su, G. D. Li, X. H. Li, and J. S. Chen, Adv. Sci. **6**, 1801702 (2019).
[34]R. Meng, X. Sun, J. Jiang, Q. Liang, Q. Yang, and X. Chen, Appl. Surf. Sci. **427**, 554 (2018).
[35]K. Ren, Y. Luo, J. Yu, and W. Tang, Chem. Phys. **528**, 110539 (2020).
[36]G. Wang, W. Tang, L. Geng, Y. Li, B. Wang, J. Chang, and H. Yuan, Phys. Status Solidi B **257**, 1900663 (2019).
[37]G. Wang, Y. Li, L. Zhang, J. Chang, Y. Li, L. Xia, S. Xiao, S. Dang, and C. Li, RSC Adv. **9**, 036234 (2019).
[38]G. Kresse and J. Furthmüller, Phys. Rev. B **54**, 11169 (1996).
[39]P. E. Blöchl, Phys. Rev. B **50**, 17953 (1994).
[40]S. Grimme, J. Antony, S. Ehrlich, and H. Krieg, J. Chem. Phys. **132**, 154104 (2010).
[41]Z. Zhang, R. Cao, C. Wang, H.-B. Li, H. Dong, W.-h. Wang, F. Lu, Y. Cheng, X. Xie, H. Liu, K. Cho, R. Wallace, and W. Wang, ACS Appl. Mater. Interfaces **7**, 5141 (2015).
[42]V. Wang, N. Xu, J. C. Liu, G. Tang, and W. Geng, arXiv:1908.08269 (2019).
[43]J. P. Perdew, K. Burke, and M. Ernzerhof, Phys. Rev. Lett. **77**, 3865 (1996).
[44]J. Heyd, J. E. Peralta, G. E. Scuseria, and R. L. Martin, J. Chem. Phys. **123**, 174101 (2005).
[45]J. Heyd, G. E. Scuseria, and M. Ernzerhof, J. Chem. Phys. **124**, 219906 (2006).
[46]Y. Liao, Z. Zhang, Z. Gao, and M. Hua, "Tunable properties of novel Ga2O3 monolayer for electronics and optoelectronics applications: A first-principles study" (unpublished) (2020).
[47]T. Björkman, A. Gulans, A. V. Krasheninnikov, and R. M. Nieminen, Phys. Rev. Lett. **108**, 235502 (2012).
[48]P. Zhang, J. Zhang, and J. Gong, Chem. Soc. Rev. **43**, 4395 (2014).
[49]H. Guo, Z. Zhang, Y. Guo, Z. Gao, R. Zheng, and H. Wu, Appl. Surf. Sci. **505**, 144650 (2020).
[50]G. Henkelman, A. Arnaldsson, and H. Jónsson, Comput. Mater. Sci. **36**, 354 (2006).
[51]Z. Gao, Z. Zhou, and D. Tománek, ACS Nano **13**, 5103 (2019).
[52]E. A. Kraut, R. W. Grant, J. R. Waldrop, and S. P. Kowalczyk, Phys. Rev. Lett. **44**, 1620 (1980).
[53]Z. Zhang, Y. Guo, and J. Robertson, Appl. Phys. Lett. **114**, 161601 (2019).
[54]M. M. Ugeda, A. J. Bradley, S.-F. Shi, F. H. Da Jornada, Y. Zhang, D. Y. Qiu, W. Ruan, S.-K. Mo, Z. Hussain, Z.-X. Shen, F. Wang, S. G. Louie, and M. F. Crommie, Nat. Mater. **13**, 1091 (2014).
[55]Y. Li, N. Stolte, B. Li, H. Li, G. Cheng, D. Pan, and J. Wang, Nanoscale **11**, 13552 (2019).
[56]G. Cheng, B. Li, C. Zhao, X. Yan, H. Wang, K. M. Lau, and J. Wang, Nano Lett. **18**, 5640 (2018).